Acceleration-Performance Optimization for Motors With Large Air Gaps

Philipp Karutz, *Student Member, IEEE*, Thomas Nussbaumer, *Member, IEEE*, Wolfgang Gruber, *Student Member, IEEE*, and Johann W. Kolar, *Senior Member, IEEE*

***Abstract*—This paper presents an optimization-procedure yielding for minimal acceleration times for different speed ranges using the example of a magnetically levitated slice motor with a large air gap. The optimization is based on a set of analytical equations together with selected 3-D finite element method simulations with the aim to optimize both the stator geometry and the number of drive turns. It is shown that the use of 3-D instead of 2-D simulation tools is obligatory for motors with large air gaps for achieving sufficient simulation accuracy. The relevant equations for the optimization are derived, and the accuracy of the proposed method is verified by measurements on a prototype system.**

***Index Terms*—Acceleration, large air gaps, magnetic levitation, permanent magnets, synchronous machines, yield optimization.**

NOMENCLATURE

d_a	Outside rotor diameter.
d_{tooth}	Air gap between stator teeth.
E	Rotational energy.
f_{el}	Electrical frequency.
I_d	Drive current.
$I_{\mathrm{pe,max}}$	Maximum output current of power electronics.
J	Inertia.
$k_{\mathrm{bemf(,sim)}}$	(Simulated) back-electromotive force (EMF) constant.
L_d	Drive-winding inductance.
$L_{d,\mathrm{sim}}$	Simulated drive-winding inductance.
m	Number of drive phases.
m_{rotor}	Rotor mass.
N_c	Number of turns per coil.
N_d	Number of turns per drive phase.
$N_{d,0}$	Number of turns for 3-D simulation results.
$N_{d,\mathrm{opt}}$	Optimal number of turns.
n_r	Rotational speed.
n_{r1}, n_{r2}	Integration boundaries of the rotational speed.
p	Number of pole pairs.
P_d	Electrical motor power.
P_{mech}	Mechanical power.
R_d	Drive-winding resistance.
t_{acc}	Acceleration time.
$T_{m,2d}$	Motor torque derived from 2-D simulations.
$T_{m,3d}$	Motor torque derived from 3-D simulations.
$U_{\mathrm{bemf(,sim)}}$	(Simulated) back EMF.
U_{dc}	DC-link voltage.
w_{tooth}	Stator tooth width.
δ_{mag}	Magnetic air gap.
δ_{mech}	Mechanical air gap.
Δn_r	Rotational-speed span.
η	Motor efficiency.
Θ_d	Drive ampere turns.
λ	Power factor.
Φ	Flux.
ω	Electrical angular frequency.

Manuscript received January 5, 2009; revised June 15, 2009. First published July 6, 2009; current version published December 11, 2009.

P. Karutz is with the ETH Zurich, 8005 Zurich, Switzerland (e-mail: karutz@lem.ee.ethz.ch).

T. Nussbaumer is with Levitronix GmbH, 8005 Zurich, Switzerland (e-mail: nussbaumer@levitronix.com).

W. Gruber is with the Austrian Center of Competence in Mechatronics GmbH, Johannes Kepler University, 4040 Linz, Austria (e-mail: wolfgang.gruber@jku.at).

J. W. Kolar is with the Power Electronic Systems Laboratory, ETH Zurich, 8092 Zurich, Switzerland (e-mail: kolar@lem.ee.ethz.ch).

Color versions of one or more of the figures in this paper are available online at http://ieeexplore.ieee.org.

Digital Object Identifier 10.1109/TIE.2009.2026376

I. INTRODUCTION

ELECTRIC motors with large air gaps are deployed in many industry applications. For example, linear induction motors that are widely used in positioning systems are characterized by air gaps of several millimeters [1]. Rotating motors with large air gaps are used when an encapsulation of the revolving rotor with a chamber is demanded. The encapsulation can be needed for protection of the equipment (e.g., in audio–visual equipment [2] or for underwater thrusters [3]) or to separate different media from each other (e.g., in vacuum systems [4] and pump applications [5]).

New emerging application fields can be identified for processing-industry branches that demand high purity (e.g., pharmaceutical and semiconductor industry). Here, the high-purity specifications can only be guaranteed by avoiding all sources that generate particles, including the mechanical bearings. Therefore, magnetically levitated motors with large air gaps are advantageously employed for these applications (cf. [6] and [7]).

The acceleration capability of such motors is crucial when they are operated in start–stop mode, as in the case in processing-industry branches. Here, the resulting acceleration time dictates the capacity of the equipment and, eventually, the cost–benefit ratio. The challenge of the motor design is therefore the maximization of the acceleration capability of the motor while having large air gaps that allow the insertion of the separating chamber wall.

Although several publications on large-air-gap motors exist [2]–[5], they do not explicitly treat the parameter and geometry optimization for maximum acceleration capability. Separate design guidelines considering the influence of the number of turns per drive phase [6] and the geometrical shape of the stator [7] on the acceleration performance of the motor have been presented in the past, not accounting for the interdependence between these two parameters. Therefore, this paper combines both parameters in an overall optimization and verifies the results on a prototype system used as an example.

The prototype system and its principle of operation are explained in Section II. The physical and mathematical background for the calculation of the acceleration performance and the description of the optimization parameters are performed in Section III. The optimization procedure and its results are described in Section IV, and the experimental verification of the results is presented in Section V.

II. Prototype System

The prototype system [7] used as an example in this paper has a mechanical air gap of 7 mm, which is a good representation of a large air gap. Since its drive is completely decoupled from the active magnetic-bearing part, the following consideration can also be applied to motor configurations with mechanical bearings.

However, the magnetic bearing offers some major advantages over mechanical bearings that are crucial for the application at hand. The advantages are almost unlimited life time, adjustable bearing parameters allowing for an active unbalance compensation (consequently avoiding processor-time costly eccentricity-detection methods presented in [8] and [9]), and wearless and lubrification-free operation, resulting in a high level of purity. Furthermore, due to the built-in fault diagnostics of the magnetic bearing [10], costly motor ball-bearing-failure detection methods as presented in [11] and [12] can be omitted.

A simplified schematic view of the prototype system is shown in Fig. 1. It combines a two-phase homopolar magnetic bearing and a two-phase permanent-magnet synchronous drive on two circumferentially shifted positions and axially different height levels. Unlike conventional bearingless motors [13], the drive and bearing units of the prototype system are completely magnetically decoupled due to their spatial and axial arrangement.

The magnetic bearing consists of two perpendicular bearing phases with the bearing permanent magnets (biasing the air-gap flux density) and the bearing windings. A current through the bearing windings will alter the air-gap flux density and therefore allow the active radial-position control, while the axial position is passively stabilized. For the sake of brevity, a more detailed description of the magnetic bearing and the levitation mechanisms is omitted, but the interested reader is referred to [14].

The drive is implemented as a permanent-magnet synchronous machine with surface-mounted magnets on the rotor, as described in [15]. This type of machine is characterized through higher efficiency and lower rotor inertia when compared with cage-type motors [16]. A detailed schematic cut view of the drive part is shown in Fig. 2, showing the round permanent magnets with alternating magnetization direction that are fixed to the rotor back iron. For the sake of brevity, the sizing of the geometrical parameters, such as drive-segment opening angle or back-iron thickness, is omitted, but the interested reader is again referred to [14].

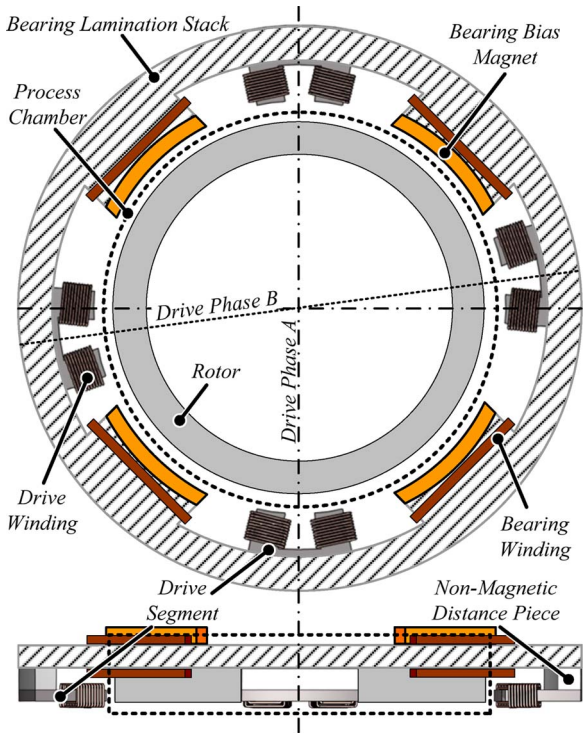

Fig. 1. Schematic top view and side view of the prototype system showing the circumferential separation of the drive and bearing unit.

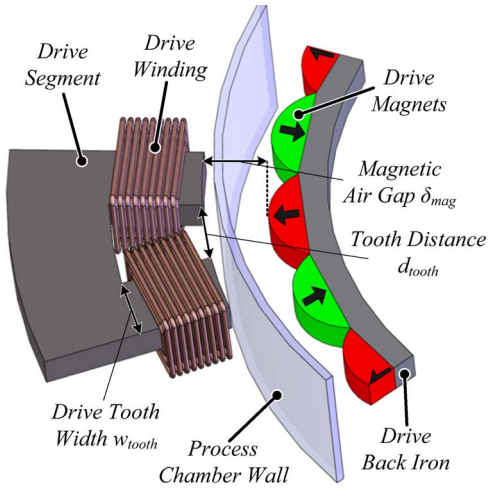

Fig. 2. Schematic cut view showing the arrangement of the concentrated windings, the air gap intersected by the process chamber wall, and the rotor in the inside of the chamber.

The drive unit consists of four separate drive segments with concentrated windings (advantageous in terms of torque density and fault tolerance [17]) that are located between the bearing units. This stator geometry is usually utilized when the circumferential space has to be used efficiently while ensuring a low-profile height as in [18]. In the case of the prototype

system, a large portion of the circumferential space is already allocated by the bearing unit (cf. Fig. 1), and the separation of the bearing and drive unit has to be guaranteed. A full circumferential drive would disturb the position control, which has to be compensated by increasing the axial distance between the bearing and drive unit, leading to a less-compact design.

Considering the need for high acceleration capability up to high rotational processing speeds (several thousand revolutions per minute) along with the large air gap (approximately 5–10 mm) demands a high drive current in the concentrated windings. Therefore, an appropriate design of the drive segments (cf. Fig. 2) avoiding possibly occurring saturation effects that increase the effective acceleration time is crucial. The effective acceleration is further influenced by the number of drive turns [6], since the inductive voltage drop limits the maximum drive current for higher rotational speeds.

The aforementioned mechanisms influence each other and have to be considered simultaneously. Therefore, in this paper, an optimization procedure is developed that allows the optimal selection of the drive-segment dimensions and the number of turns in dependence on the speed range. This is based on the general physical dependences of the machine that will be explained in the subsequent section. Since the flux density in the stator segments depends on the highly nonlinear flux distribution, this optimization is supported by the results of 3-D finite element method (FEM) simulations.

Although the prototype system incorporates a magnetic bearing, it is not part of the optimization due to the complete magnetic decoupling of the bearing and drive unit. However, the magnetic bearing provides the technical constraints leading to the unconventional stator structure. Even though this stator structure tends to saturation more likely than full circumferential stators, the methods and mechanisms presented in this paper can be adopted for other stator structures.

III. Physical and Mathematical Background

The example prototype system is controlled through field-oriented control, which is a commonly applied control scheme for state-of-the-art motors [15]. Therefore, the drive windings are fed with an appropriate current I_d that is kept in phase with the back EMF U_{bemf}. The control of the motor is implemented using a cascaded control with the drive-current controller in the inner loop and the rotational-speed controller in the outer loop. The drive current I_d in each of the two phases can be controlled independently through the employment of a standard full-bridge inverter topology with four bridge legs, as shown in Fig. 3.

The drive phases are modeled by the equivalent electrical circuits shown in Fig. 3. The lumped elements account for the winding inductance L_d, the winding resistance R_d, and the peak value of the back EMF $\hat{U}_{\mathrm{bemf}}$ per phase. As shown in [6], applying Kirchhoff's law to the equivalent electrical circuit and solving for the peak drive current $\hat{I}_d$ gives

$$\hat{I}_d = \frac{-\hat{U}_{\mathrm{bemf}} \cdot R_d \pm \sqrt{\left(R_d^2 + \omega^2 \cdot L_d^2\right) U_{\mathrm{dc}}^2 - \omega^2 \cdot L_d^2 \cdot \hat{U}_{\mathrm{bemf}}^2}}{R_d^2 + \omega^2 \cdot L_d^2} \tag{1}$$

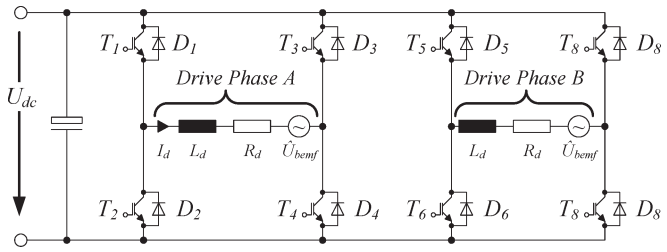

Fig. 3. Two-phase drive inverter topology consisting of two full-bridge circuits.

with the dc-link voltage U_{dc} and the electrical angular frequency ω. From (1), the current-limiting effect of the inductive voltage drop and the back EMF becomes obvious.

To derive the acceleration time of the motor for a certain speed span, the approach of [6] is applied. With the electrical motor power P_d being defined as

$$P_d = m \cdot U_{\mathrm{bemf}} \cdot I_d \tag{2}$$

FD2 with the number of drive phases m, a change in rotational energy E of the rotor within a time step dt is given by

$$dE = P_d \cdot dt = m \cdot U_{\mathrm{bemf}} \cdot I_d \cdot dt. \tag{3}$$

Here, the rotational energy is calculated by

$$E = \frac{1}{2} \cdot J \cdot \left(\frac{2\pi}{60}\right)^2 \cdot n_r^2 \tag{4}$$

with the inertia J and the rotational speed n_r. Combining (2)–(4) results in the required acceleration time t_{acc} between two rotational speed values n_{r1} and n_{r2}

$$t_{\mathrm{acc}} = \frac{J \cdot n_r}{m \cdot U_{\mathrm{bemf}}} \cdot \left(\frac{2\pi}{60}\right)^2 \cdot \int_{n_{r1}}^{n_{r2}} \frac{1}{I_d(n_r)} dn_r. \tag{5}$$

Judging from (5), a minimum acceleration time t_{acc} can be obtained if both U_{bemf} and I_d are maximized. The back EMF U_{bemf} can be described as

$$U_{\mathrm{bemf}} = N_d \cdot \frac{d\Phi}{dt} \tag{6}$$

with the number of turns per drive phase N_d and the flux Φ, which originates from the permanent magnets and passes through the stator-drive segments. The back EMF can be generally maximized in three ways.

First, U_{bemf} is directly proportional to the number of drive turns N_d [cf. (6)], which should therefore be as large as possible.

Second, the flux linkage Φ and, therefore, U_{bemf} is increased by a large cross-sectional area of the drive teeth facing the drive permanent magnets. This ensures a small flux density impressed by the permanent-magnet field and, therefore, little tendency to iron saturation, which would effectively lower the flux linkage. In particular, the drive tooth width w_{tooth} (cf. Fig. 2) shall be maximized. An increase of the tooth height is not fulfilling the demand for a compact setup (as the rotor height would have to be increased as well, which would result

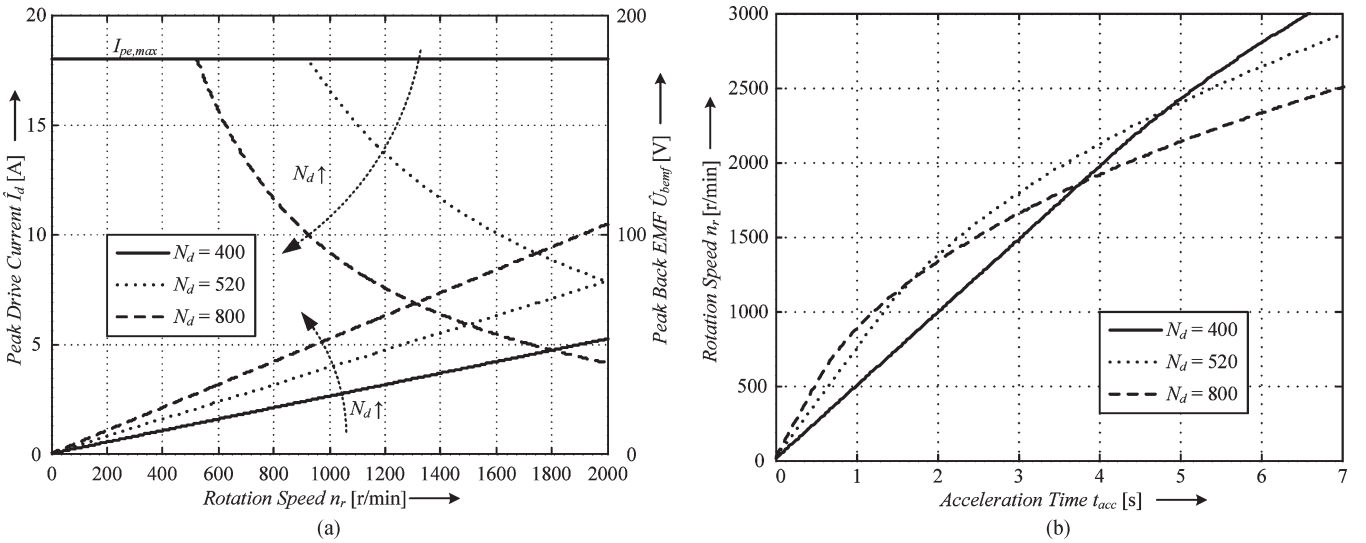

Fig. 4. (a) Achievable drive current $\hat{I}_d$ (for $I_{\mathrm{pe,max}} = 18$ A) and back EMF $\hat{U}_{\mathrm{bemf}}$ in dependence of the rotational speed n_r for different numbers of turns per drive phase N_d. (b) Estimated acceleration performance for the prototype system.

in a larger inertia and a worse acceleration performance, respectively). Thus, from the viewpoint of maximum flux linkage, the tooth width w_{tooth} should be chosen as large as possible.

However, a third effect occurs, which is the saturation of the stator segments caused by the impressed ampere turns. In [7], it has been shown that the drive-segment shape influences the inclination of the iron to saturate for certain levels of drive ampere turns Θ_d, being defined as

$$\Theta_d = N_d \cdot I_d. \tag{7}$$

For large tooth widths (as they are desired for high flux linkage), the air gap between the stator teeth d_{tooth} (cf. Fig. 2) may get small enough to saturate the iron for high ampere turns and degrade the flux linkage and, consequently, the effective torque (the flux caused by the stator current mainly passes between the drive teeth due to the large air gap between rotor and stator and the airlike permeability of the permanent magnets).

Hence, to avoid this saturation, the tooth width w_{tooth}, the number of drive turns N_d, and the drive current I_d should be chosen as small as possible. Obviously, this is contradictory to all the aforementioned considerations, which already shows that it is indispensable to take all these effects into account to achieve optimum acceleration performance.

An additional issue that has to be considered for the optimization is the limitation of the feasible drive current I_d, as shown in (1). Here, the resistive voltage drop is included only for the sake of completeness, but it has typically only a minor influence on the resulting drive current. Typical drive-current characteristics in dependence of the rotational speed n_r are shown in Fig. 4(a). For low rotational speeds n_r, the drive current is limited to the maximum output current of the power electronics inverter $I_{\mathrm{pe,max}}$, since the influence of the back EMF and inductive voltage drop is still low. The current starts to decrease at a certain rotational speed depending on the number of drive turns. Therefore, to maximize the current, the back EMF $\hat{U}_{\mathrm{bemf}}$ and the drive phase inductance L_d should be reduced, which are both dependent on the number of turns N_d and the tooth width w_{tooth}, as explained before.

High rotational speeds can alternatively also be reached by applying flux-weakening control as presented in [19]. Here, the current-limiting effect of the back EMF is reduced by active field weakening. However, this control will not lead to a minimal acceleration time.

According to (5), the acceleration time t_{acc} depends on the reciprocal product of the drive current I_d and the back EMF, which demands for an optimization of the drive number of turns N_d and the tooth width w_{tooth} to achieve maximum torque.

As an example, the dependence of the acceleration time t_{acc} on the drive number of turns N_d for different rotational speeds n_r is shown in Fig. 4(b). Comparison of the three curves shows that the fastest acceleration ($t_{\mathrm{acc}} = 3.5$ s) toward a rotational speed of $n_r = 2000$ r/min can be accomplished by the employment of a number of drive turns of $N_d = 520$. For lower rotational speeds, higher number of drive turns would be more appropriate, and the same applies inversely for higher rotational speeds.

Hence, the minimization of the acceleration time as a measure for the drive torque has to be carried out also considering the rotational-speed span $\Delta n_r = n_{r2} - n_{r1}$, since it is shifting the optimization point of the design. To maximize the overall acceleration capability, an optimization considering the drive tooth width w_{tooth}, the number of drive turns N_d, and the rotational-speed span Δn_r has to be accomplished. A description of this optimization routine is given in the next section.

IV. Optimization Routine

A three-loop optimization procedure, as shown in Fig. 5, was developed to determine the optimal sizing parameters (tooth width w_{tooth} and number of drive turns N_d) for a minimal acceleration time t_{acc} within a certain rotational-speed span Δn_r.

Since the flux distribution in the air gap is highly nonlinear and the aforementioned saturation effects shall be considered in the optimization procedure, an analytical derivation of the back EMF and the drive inductance is imprecise.

Therefore, as shown in Fig. 5, the optimization procedure uses the results of 3-D FEM simulations [21] of the simulated

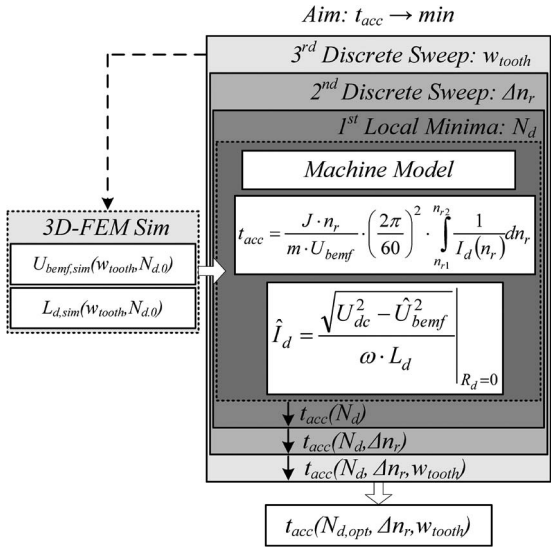

Fig. 5. Optimization procedure for maximum acceleration capability, showing three loops of parameter sweeping with 3-D FEM simulation data being used in the analytical machine model.

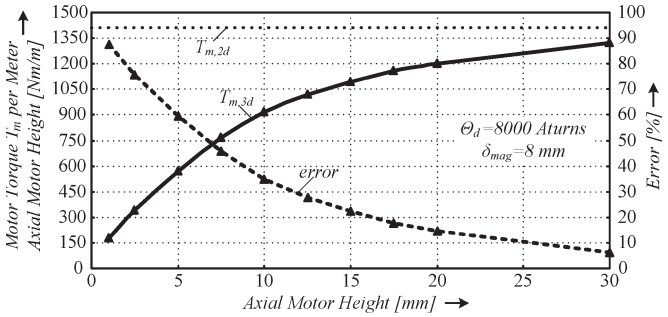

Fig. 6. Comparison of the 2-D ($T_{m,2d}$) and 3-D ($T_{m,3d}$) simulation results of the motor torque shown as a function of the axial motor height for 8000 A and a magnetic air gap δ_{mag} of 8 mm. The percentage aberration (*error*) between both curves is indicated.

back EMF $U_{\mathrm{bemf,sim}}$ and the effective drive inductance L_{sim} in dependence on $N_{d,0}$ and w_{tooth}. A step-by-step motor design through variation of geometry parameters within an FEM simulation is a commonly used method according to [22]. Even design methods based on analytical approaches are nowadays usually validated employing FEM simulation methods [23].

A 3-D simulation tool was chosen for the analysis at hand to consider the occurring effects in the proximity of iron saturation that are effectively lowering the resulting torque.

These effects are not considered by 2-D simulations. This fact is illustrated in Fig. 6. From the 2-D simulation, a torque-per-meter value $T_{m,2d}$ is obtained that is shown in comparison with the equivalent 3-D simulation result $T_{m,3d}$. In particular, for a small axial motor height and/or for large air gaps, the 2-D simulation delivers results with large errors. For the prototype system with an axial height of 10 mm and a magnetic air gap of 8 mm, this would result in an error of around 35%, which is not acceptable for the optimization.

Naturally, the quantity of the error is influenced by the geometrical parameters (air gap δ, stator height) and the degree of saturation (adjustable through Θ_d). A complete analysis of this phenomenon is omitted for the sake of brevity, but will be

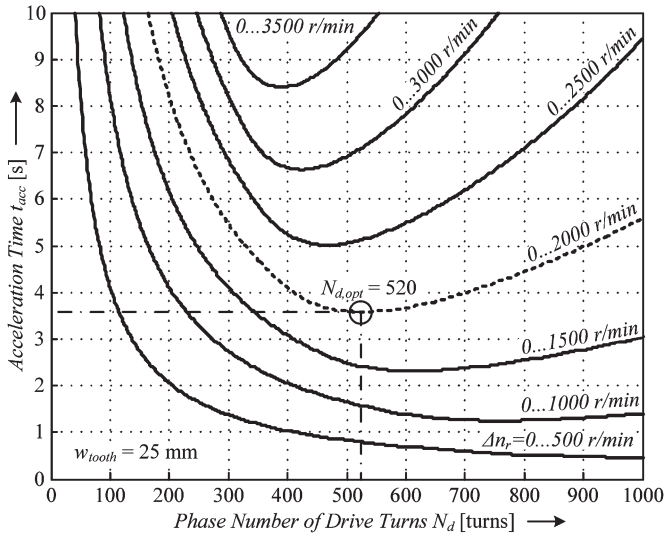

Fig. 7. Dependence of the acceleration time t_{acc} on the phase drive number of turns N_d presented for a constant drive tooth width $w_{\mathrm{tooth}} = 25$ mm and different rotational-speed spans Δn_r. The optimal number of turns $N_{d,\mathrm{opt}}$ is indicated as an example for an acceleration from 0 to 2000 r/min.

dealt with in a separate paper. However, Fig. 6 illustrates that, for this motor type, only 3-D simulations are applicable.

Equations (1) and (5) are used as a machine model and are applied in the optimization procedure to calculate the time behavior of the drive current I_d and, consequently, the acceleration time t_{acc} for a certain speed span Δn_r of the drive, similar to Fig. 4.

In the first loop, only the number of drive turns N_d is varied, and the parameters tooth width w_{tooth} and speed range Δn_r are left constant. Since $U_{\mathrm{bemf,sim}}$ and $L_{d,\mathrm{sim}}$ are obtained for a specified number of turns $N_{d,0}$, they have to be rescaled for every new N_d by the following equations:

$$L_d = L_{d,\mathrm{sim}} \cdot \left(\frac{N_d}{N_{d,0}}\right)^2 \tag{8}$$

$$U_{\mathrm{bemf}} = U_{\mathrm{bemf,sim}} \cdot \left(\frac{N_d}{N_{d,0}}\right). \tag{9}$$

The repetitive variation of the number of drive turns N_d in a reasonable range and the recording of the corresponding acceleration time result in a single curve of Fig. 7 (cf. dotted line). As an example, the optimal number of turns $N_{d,\mathrm{opt}} = 520$ for a minimal acceleration time of $t_{\mathrm{acc}} = 3.5$ s during an acceleration from 0 up to 2000 r/min, and a tooth width of $w_{\mathrm{tooth}} = 25$ mm is shown in Fig. 7.

The second loop adds the variation of the rotational-speed range Δn_r into the optimization procedure, which delivers multiple curves similar to the dotted one from the first loop. These curves result in the array of curves shown in Fig. 7 (for the sake of illustration, the rotational-speed span is varied in 500-r/min steps). For each of the curves, there exists an optimal number of turns $N_{d,\mathrm{opt}}$. Here, the tendency toward lower N_d for higher Δn_r is already visible.

Finally, the variation of the tooth width through the variation of the source simulation data is implemented into the third loop. As a result, various curve arrays as shown in Fig. 7 are generated for different tooth widths, where for each

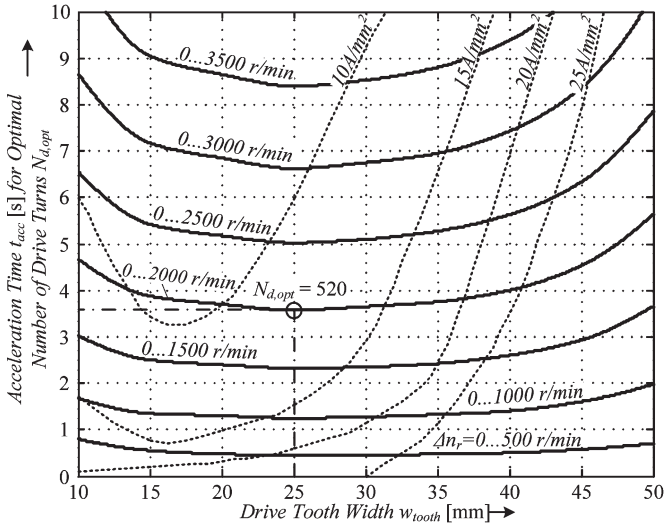

Fig. 8. Optimization result showing the acceleration time t_{acc} with the optimal number of turns $N_{d,\mathrm{opt}}$ in dependence of the tooth width w_{tooth} and the rotational-speed range Δn_r The dotted lines indicate areas of different occurring current densities within the drive-winding wire.

combination of Δn_r and w_{tooth}, the optimal number of turns can be determined.

In Fig. 8, the resulting acceleration time for different tooth widths is shown whereby each point is characterized by the optimal number of turns $N_{d,\mathrm{opt}}$. Generally, the tooth width $w_{\mathrm{tooth}} = 25$ mm shows the lowest acceleration times for the shown speed ranges. Around this optimum, the time difference is rather low, provided the corresponding optimal drive number of turns is implemented.

However, as stated before, the acceleration time rises rapidly for significantly smaller and larger values of w_{tooth}. This is due to the effect that small tooth widths demand higher number of turns due to the reduced coil flux linkage and the occurring saturation effects. For larger values of w_{tooth}, the magnetic resistance between the teeth decreases, which augments the tendency for saturation of the teeth and consequently lowers the effective torque. Additionally, the limited space between the teeth increases the current density in the wires of the drive winding, since for a given optimal number of turns, the diameter has to be reduced.

In Fig. 8, this effect is addressed by the dotted lines defining different areas of current density. Hence, particularly for the motor at hand and the targeted rotational-speed span up to 2000 r/min, tooth widths larger than 30 mm seem inappropriate due to resulting high thermal stress of the drive windings.

From the results of the presented optimization procedure, the tooth width $w_{\mathrm{tooth}} = 25$ mm with an optimal number of turns number $N_{d,\mathrm{opt}} = 520$ was implemented in an experimental prototype. The next section presents the results of the experimental verification.

V. Experimental Verification

The laboratory prototype used for the experimental verification is shown in Fig. 9, and the main parameters are summarized in Table I.

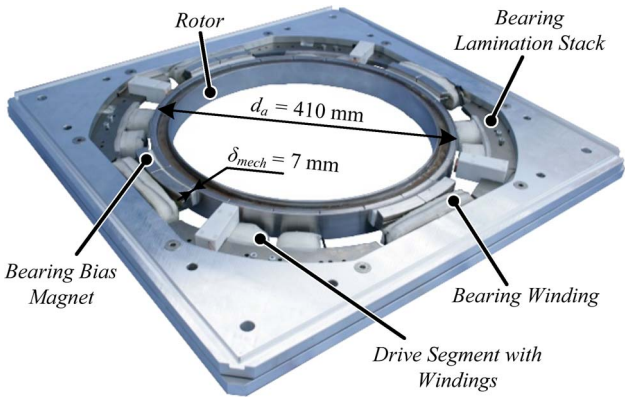

Fig. 9. Laboratory prototype used for the experimental verification measurements employs two drive phases. Each drive phase consists of two drive segments with $w_{\mathrm{tooth}} = 25$ mm, and each drive segment has two coils with the number of turns per coil of $N_c = N_d/4 = 130$ turns.

TABLE I
Design Data of Experimental Setup

Outside rotor diameter d_a	410 mm
Mechanical air gap δ_{mech}	7 mm
Number of pole pairs p	12
Specified rotation speed span Δn_r	2000 r/min
Optimal number of drive turns $N_{d,opt}$	520
Acceleration time t_{acc} for Δn_r	3.5 s
Rotor mass m_{rotor}	5 kg

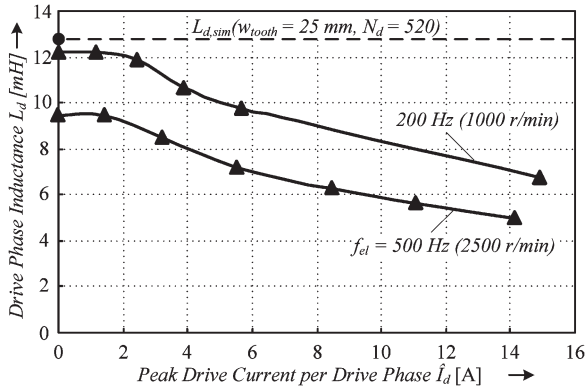

Fig. 10. Drive inductance L_d in dependence of the drive current I_d and the electrical frequency f_{el} with simulated inductance L_{sim} indicated.

To verify the 3-D FEM simulation results that are used within the optimization procedure, the drive inductance L_d and the back EMF U_{bemf} have been derived from measurements on the prototype. In Fig. 10, the drive phase inductance L_d is shown in dependence of the drive current I_d for two different frequencies. The inductance values were obtained through phase-shift measurements between sinusoidal voltage and current, fed in by a linear power amplifier. Here, the inductance values decrease for higher frequencies and also for increasing drive current I_d due to the occurring saturation effects in the stator iron. In the proposed optimization scheme, neither the current nor the frequency dependence has been considered, since it is based only on one single simulation result. Obviously, by regarding

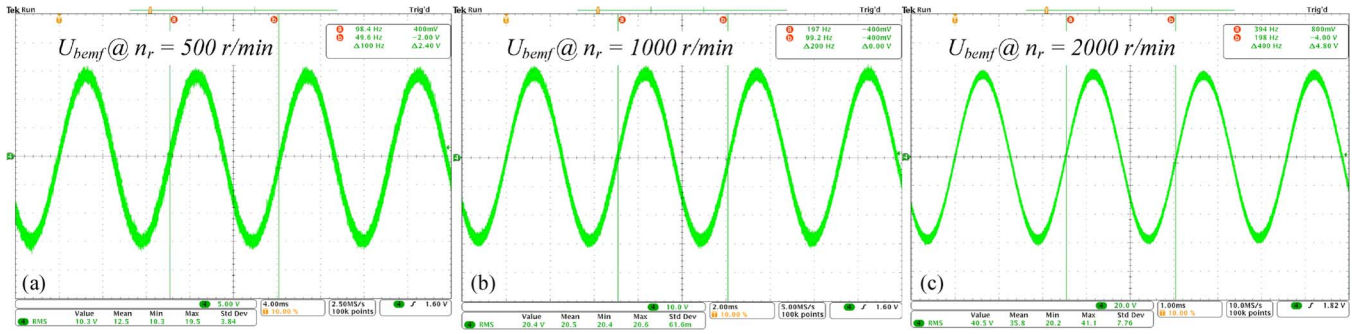

Fig. 11. Back EMF U_{bemf} of one drive phase for three different rotational speeds resulting in a back EMF constant $k_{\mathrm{bemf}} = 0.039$ mV rms/(r/min) per turn (for a drive number of turns of $N_d = 520$) (scales: (a) 5 V/div, 4 ms/div; (b) 10 V/div, 2 ms/div; (c) 20 V/div, 1 ms/div.

Fig. 10, it becomes clear that this is a simplification, which is not valid for high currents and/or frequencies. However, the value obtained by 3-D FEM simulations has a good accordance with the experimental value for low frequencies and low current. Since this is the maximum occurring value (and low inductance is desired in terms of acceleration), the simulation result represents a good worst-case consideration.

The second value that was obtained through the 3-D FEM simulations is the back EMF U_{bemf} that was verified on the prototype through measurements on an open drive coil. In Fig. 11 the corresponding waveforms are shown for different rotational speeds, and a resulting back EMF constant k_{bemf} being defined as

$$k_{\mathrm{bemf}} = \frac{U_{\mathrm{bemf}}}{n_r \cdot N_d} \tag{10}$$

of $k_{\mathrm{bemf}} = 0.039$ mV rms/(r/min) per turn was determined. This value is practically constant for all considered rotational speeds and shows a good match with $k_{\mathrm{bemf,sim}} = 0.041$ mV, which is the 3-D FEM result. The accordance of the simulated and real values is needed to obtain optimization parameters with low error when compared with the real acceleration behavior of the motor.

Due to the cost and work efforts involved with the manufacturing of a stator segment including the drive windings, only the optimal point for the specified rotational-speed span of $\Delta n_r = 2000$ r/min is verified. Correspondingly, an acceleration behavior of the motor is shown in Fig. 12. Here, the rotational speed of $n_r = 2000$ r/min is reached within $t_{\mathrm{acc}} = 3.5$ s. The comparison of this measurement with the optimal point shown in Fig. 8 shows a very good accordance. This demonstrates that the method for the acceleration-capability maximization is precise and applicable for the motors at hand.

From Fig. 12, the deceleration time can be identified to be smaller than the acceleration time. This is due to the fact that the sign of the drive current I_d changes with respect to the back EMF U_{bemf}, which now acts against the resistive voltage drop. That is, for deceleration, the sign of $\hat{U}_{\mathrm{bemf}} \cdot R_d$ in (1) has to be changed, which allows a higher current and, consequently, a reduced deceleration time.

Finally, efficiency and power-factor measurements have been carried out for the motor prototype. The characterization of a motor through efficiency measurements is a standard procedure in drive design. However, due to the rotor geometry

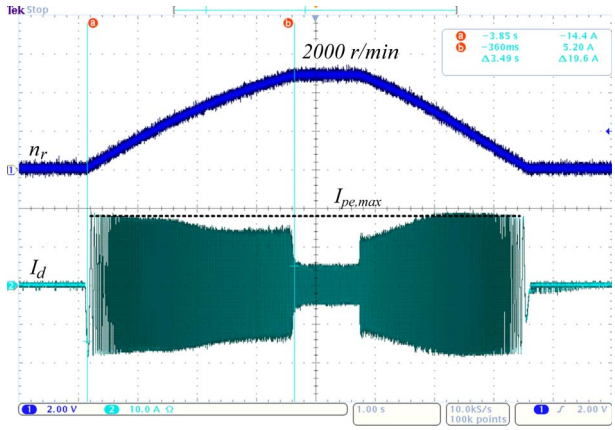

Fig. 12. Acceleration behavior of the laboratory prototype from 0 to 2000 r/min for a maximum current limited by the power electronics to $I_{\mathrm{pe,max}} = 18$ A (with number of turns per drive coil $N_c = N_d/4 = 130$, this results in a maximum ampere turns value per stator element with two coils of $\Theta_d = 4680$ A) in 3.5 s, and deceleration in 2.6 s (scales: 800 (r/min)/div, 10 A/div, 1 s/div).

and the magnetic levitation, it is not possible to connect a torque transducer to the rotor as commonly done for standard machines. The torque is therefore obtained by an integrative method based on the following equation:

$$T_d = J \cdot \frac{2\pi}{60} \cdot \frac{\Delta n_r}{\Delta t}. \tag{11}$$

With this method, only the rotational speed n_R has to be measured over time during acceleration to determine the mechanical power P_{mech} of a rotor with a known inertia J according to

$$P_{\mathrm{mech}} = T_d \cdot \frac{2\pi}{60} \cdot n_r. \tag{12}$$

The mechanical power is then compared with the electrical power, which can commonly be determined through voltage and current measurements at the motor and/or inverter input terminals (whereby, in the latter case, the inverter efficiency has to be taken into account). With this method, the dynamic efficiency during acceleration can be determined, which is the relevant performance parameter, since the motor does require most power at these transient conditions.

The resulting motor efficiency for different rotational speed values up to 2000 r/min is presented in Fig. 13, along with the power factor measured at the input terminals of the inverter.

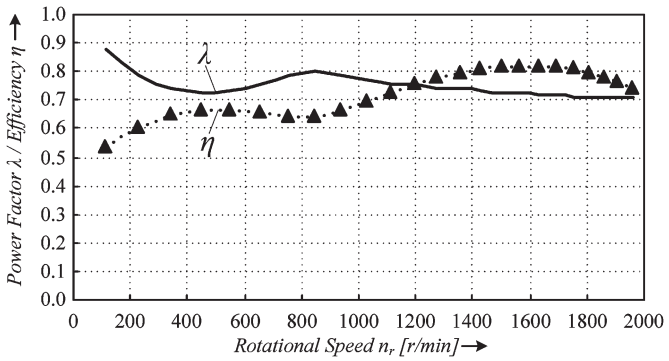

Fig. 13. Motor efficiency η and power factor λ of the prototype system in dependence of the rotational speed n_r.

VI. Conclusion

In this paper, an optimization procedure aiming for minimal acceleration time for motors with large air gaps has been presented. The physical background describing the limitations of the acceleration capability has been explained, and the main analytical equations have been derived. These equations have been implemented into a three-loop optimization procedure that uses 3-D FEM simulation results for an overall minimization of the acceleration time. It has been demonstrated that the use of 3-D instead of 2-D FEM simulation tools is important particularly for motors with large air gaps to achieve appropriate simulation accuracy. A prototype system has been used to verify the optimization results, which shows a good accordance with the measurements. In the same manner, this method can also be applied to other motor topologies to predict and optimize their acceleration capability.

References

[1] G. Kang, J. Kim, and K. Nam, "Parameter estimation scheme for low-speed linear induction motors having different leakage inductances," *IEEE Trans. Ind. Electron.*, vol. 50, no. 4, pp. 708–716, Aug. 2003.

[2] M. Sanada, S. Morimoto, and Y. Takeda, "Axial type flat PM motor with large air gap," in *Proc. Power Convers. Conf.*, Nagaoka, Japan, 1997, vol. 2, pp. 643–647.

[3] S. Sharkh, S. Lai, and S. Turnock, "Structurally integrated brushless PM motor for miniature propeller thrusters," in *Proc. Inst. Elect. Eng.—Elect. Power Appl.*, Sep. 2004, vol. 151, no. 5, pp. 513–519.

[4] M. Poloujadoff, J. Laeuffer, J. Obadia, and N. Rezgui, "Rotor speed and temperature measurement in a large air gap induction motor," in *Conf. Rec. 30th IEEE IAS Annu. Meeting*, 1995, vol. 1, pp. 625–628.

[5] S.-M. Yang and C.-C. Lin, "Performance of a single-axis controlled magnetic bearing for axial blood pump," in *Conf. Rec. 42nd IEEE IAS Annu. Meeting*, 2007, pp. 963–968.

[6] T. Schneeberger, T. Nussbaumer, and J. W. Kolar, "Magnetically levitated homopolar hollow-shaft motor," *IEEE/ASME Trans. Mechatronics*, to be published.

[7] P. Karutz, T. Nussbaumer, W. Gruber, and J. Kolar, "Saturation effects in high acceleration bearingless motors," in *Proc. IEEE ISIE*, 2008, pp. 472–477.

[8] M. Drif and A. Cardoso, "Airgap-eccentricity fault diagnosis, in three-phase induction motors, by the complex apparent power signature analysis," *IEEE Trans. Ind. Electron.*, vol. 55, no. 3, pp. 1404–1410, Mar. 2008.

[9] R. Andriamalala, H. Razik, L. Baghli, and F. Sargos, "Eccentricity fault diagnosis of a dual-stator winding induction machine drive considering the slotting effects," *IEEE Trans. Ind. Electron.*, vol. 55, no. 12, pp. 4238–4251, Dec. 2008.

[10] M. Sahinkaya, A. Abulrub, P. Keogh, and C. Burrows, "Multiple sliding and rolling contact dynamics for a flexible rotor/magnetic bearing system," *IEEE/ASME Trans. Mechatronics*, vol. 12, no. 2, pp. 179–189, Apr. 2007.

[11] A. Ibrahim, M. El Badaoui, F. Guillet, and F. Bonnardot, "A new bearing fault detection method in induction machines based on instantaneous power factor," *IEEE Trans. Ind. Electron.*, vol. 55, no. 12, pp. 4252–4259, Dec. 2008.

[12] M. Blodt, P. Granjon, B. Raison, and G. Rostaing, "Models for bearing damage detection in induction motors using stator current monitoring," *IEEE Trans. Ind. Electron.*, vol. 55, no. 4, pp. 1813–1822, Apr. 2008.

[13] S. Zhang and F. L. Luo, "Direct control of radial displacement for bearingless permanent-magnet-type synchronous motors," *IEEE Trans. Ind. Electron.*, vol. 56, no. 2, pp. 542–552, Feb. 2009.

[14] P. Karutz, T. Nussbaumer, W. Gruber, and J. Kolar, "Novel magnetically levitated two-level motor," *IEEE/ASME Trans. Mechatronics*, vol. 13, no. 6, pp. 658–668, Dec. 2008.

[15] K. Chau, C. Chan, and C. Liu, "Overview of permanent-magnet brushless drives for electric and hybrid electric vehicles," *IEEE Trans. Ind. Electron.*, vol. 55, no. 6, pp. 2246–2257, Jun. 2008.

[16] B. Bose, "Power electronics and motor drives recent progress and perspective," *IEEE Trans. Ind. Electron.*, vol. 56, no. 2, pp. 581–588, Feb. 2009.

[17] C. Gerada and K. Bradley, "Integrated PM machine design for an aircraft EMA," *IEEE Trans. Ind. Electron.*, vol. 55, no. 9, pp. 3300–3306, Sep. 2008.

[18] M. Tsai, M. Weng, and M. Hsieh, "Computer-aided design and analysis of new fan motors," *IEEE Trans. Magn.*, vol. 38, no. 5, pp. 3467–3474, Sep. 2002.

[19] C. Jo, J.-Y. Seol, and I.-J. Ha, "Flux-weakening control of IPM motors with significant effect of magnetic saturation and stator resistance," *IEEE Trans. Ind. Electron.*, vol. 55, no. 3, pp. 1330–1340, Mar. 2008.

[20] J. Finch and D. Giaouris, "Controlled AC electrical drives," *IEEE Trans. Ind. Electron.*, vol. 55, no. 2, pp. 481–491, Feb. 2008.

[21] *Maxwell*, Ansoft Corp., Pittsburg, Pennsylvania.

[22] Y. Li, J. Zou, and Y. Lu, "Optimum design of magnet shape in permanent-magnet synchronous motors," *IEEE Trans. Magn.*, vol. 39, no. 6, pp. 3523–3526, Nov. 2003.

[23] J. Wang, D. Howe, and G. Jewell, "Analysis and design optimization of an improved axially magnetized tubular permanent-magnet machine," *IEEE Trans. Energy Convers.*, vol. 19, no. 2, pp. 289–295, Jun. 2004.

Philipp Karutz (S'06) was born in Magdeburg, Germany, in 1981. He received the M.Sc. degree in electrical engineering at Otto-von-Guericke University Magdeburg, Magdeburg, in 2005. He has been working toward the Ph.D. degree at the Power Electronic Systems Laboratory, Swiss Federal Institute of Technology (ETH) Zurich, Zurich, Switzerland, since 2006.

Since 2005, he has been with ABB Corporate Research Centre, Baden, Switzerland, working on electromagnetic compatibility simulations/measurements and the packaging of power modules for motor drives. His research interests include power factor correction, ultracompact ac-dc converters, and magnetically levitated motors.

Thomas Nussbaumer (S'02–M'06) was born in Vienna, Austria, in 1975. He received the M.Sc. degree (with honors) in electrical engineering from the University of Technology Vienna, Vienna, Austria, in 2001, and the Ph.D. degree from the Power Electronic Systems (PES) Laboratory, Swiss Federal Institute of Technology (ETH) Zurich, Zurich, Switzerland, in 2004.

From 2001 to 2006, he was with the PES, where he conducted research on modeling, design, and control of three-phase rectifiers, power factor correction techniques, and electromagnetic compatibility. Since 2006, he has been with Levitronix GmbH, Zurich, Switzerland, where he is currently working on bearingless motors, magnetic levitation, and permanent-magnet motor drives for the semiconductor and biotechnology industry. His current research is focused on compact and high-performance mechatronic systems including novel power electronics topologies, control techniques, drive systems, sensor technologies, electromagnetic interference (EMI), and thermal aspects.

Wolfgang Gruber (S'07) was born in Amstetten, Austria, in 1977. He received the M.Sc. degree in mechatronics at Johannes Kepler University Linz, Linz, Austria, in 2004, where he has been working toward the Ph.D degree since 2004.

Since 2004, he has been a Scientific Assistant with the Institute of Electrical Drives and Power Electronics, Johannes Kepler University Linz, where he has been involved in various research projects. His research interests include magnetic bearings, bearingless motors, and brushless motors.

Mr. Gruber is a member of the Association for Electrical, Electronic and Information Technologies (VDE).

Johann W. Kolar (M'89–SM'04) received the Ph.D. degree (*summa cum laude/promotio sub auspiciis praesidentis rei publicae*) from the University of Technology Vienna, Vienna, Austria.

Since 1984, he has been working as an independent international consultant in close collaboration with the University of Technology Vienna, in the fields of power electronics, industrial electronics, and high performance drives. He has proposed numerous novel pulsewidth-modulation converter topologies, and modulation and control concepts, e.g., the Vienna Rectifier and the three-phase ac–ac sparse matrix converter. He has published over 250 scientific papers in international journals and conference proceedings and has filed more than 70 patents. He is currently with the Swiss Federal Institute of Technology, (ETH) Zurich, Zurich, Switzerland, where he was appointed Professor and Head of the Power Electronic Systems Laboratory, on February 1, 2001. The focus of his current research is on ac–ac and ac–dc converter topologies with low effects on the mains, e.g., for power supply of telecommunication systems, More-Electric Aircraft, and distributed power systems in connection with fuel cells. Further main areas of research are the realization of ultracompact intelligent-converter modules employing the latest power semiconductor technology (SiC), novel concepts for cooling, and electromagnetic-interference filtering, multidomain/multiscale modeling and simulation, pulsed power, bearingless motors, and Power microelectromechanical systems.

Dr. Kolar is a member of the Institute of Electrical Engineering in Japan (IEEJ) and of technical program committees of numerous international conferences in the field (e.g., Director of the Power Quality Branch of the International Conference on Power Conversion and Intelligent Motion). From 1997 through 2000, he served as an Associate Editor of the IEEE TRANSACTIONS ON INDUSTRIAL ELECTRONICS, and, since 2001, has served as an Associate Editor of the IEEE TRANSACTIONS ON POWER ELECTRONICS. Since 2002, he has also been an Associate Editor of the *Journal of Power Electronics* of the Korean Institute of Power Electronics and a member of the Editorial Advisory Board of the *IEEJ Transactions on Electrical and Electronic Engineering*. He is the recipient of the Best Transactions Paper Award of the IEEE Industrial Electronics Society in 2005. He was also the recipient of an Erskine Fellowship from the University of Canterbury, New Zealand, in 2003. In 2006, the European Power Supplies Manufacturers Association recognized the Power Electronics Systems Laboratory of ETH Zurich as the leading academic research institution in Europe.